Mechanostat parameters estimated from time-lapsed *in vivo* micro-computed tomography data of mechanically driven bone adaptation are logarithmically dependent on loading frequency

Francisco C. Marques[1], Daniele Boaretti[1], Matthias Walle[1], Ariane C. Scheuren[1], Friederike A. Schulte[1], Ralph Müller*[1]

[1]Institute for Biomechanics, ETH Zurich, Zurich, Switzerland

*** Correspondence:**
Ralph Müller
ram@ethz.ch

Keywords: Bone remodeling, mechanical loading, high performance computing, frequency dependency, micro-finite element analysis, mechanostat theory, mechanoregulation, mouse caudal vertebra

Abstract

Mechanical loading is a key factor governing bone remodeling and adaptation. Both preclinical and clinical studies have demonstrated its effects on bone tissue, which were also notably predicted in the mechanostat theory. Indeed, existing methods to quantify bone mechanoregulation have successfully associated the frequency of remodeling events with local mechanical signals, combining time-lapsed *in vivo* micro-computed tomography (micro-CT) imaging and micro-finite element (micro-FE) analysis. However, a correlation between the local surface velocity of remodeling events and mechanical signals has not been shown. As many degenerative bone diseases have also been linked to impaired bone remodeling, this relationship could provide an advantage in detecting the effects of such conditions and advance our understanding of the underlying mechanisms. Therefore, in this study, we introduce a novel method to estimate remodeling velocity (RmV) curves from time-lapsed *in vivo* mouse caudal vertebrae data under static and cyclic mechanical loading. These curves can be fitted with piecewise linear functions as proposed in the mechanostat theory. Accordingly, new remodeling parameters can be derived from such data, including formation saturation levels (FSL), resorption velocity modulus (RVM), and remodeling thresholds (RmT). Our results revealed that the norm of the gradient of strain energy density (∇SED) yielded the highest accuracy to quantify mechanoregulation data using micro-FE analysis with homogeneous material properties, while effective strain was the best predictor for micro-FE analysis with heterogeneous material properties. Furthermore, RmV curves could be accurately described with piecewise linear and hyperbola functions (root mean square error below 0.2 µm/day for weekly analysis) and several remodeling parameters determined from these curves followed a logarithmic relationship with loading frequency, especially FSL and RmT values for both weekly and four-weekly analysis. Crucially, RmV curves and derived parameters could detect differences in mechanically driven bone adaptation, which complemented previous results showing a logarithmic relationship between loading frequency and net change in bone volume fraction over four weeks. Together, we expect this data to support the calibration of *in silico* models of bone adaptation and the characterization of the effects of mechanical loading and pharmaceutical treatment interventions *in vivo*.

Introduction

Bone is a dynamic organ capable of adapting to its mechanical environment (Burr et al. 2002). Through a multiscale process, loads are transferred from the organ to the cellular level, eliciting highly coordinated biological responses that remodel its architecture (Wolff 1986, Lanyon 1992, Turner 1998). Indeed, several studies have successfully shown the influence of mechanical loading in bone adaptation, especially in trabecular bone, highlighting how mechanical cues guide the bone structure towards an optimal load transfer (Lanyon 1992, Rubin et al. 1994, Huiskes et al. 2000, De Souza et al. 2005, Lambers et al. 2011). From a mathematical modeling perspective, the mechanostat theory (Frost 1987) is a widely known proposal for the regulatory mechanism driving tissue-level bone adaptation, which has been successfully incorporated into *in silico* models of bone adaptation capable of approximating the trends observed *in vivo* in response to various interventions (Levchuk et al. 2014) and loading frequencies (Kameo et al. 2011). Such models can leverage time-lapsed *in vivo* micro-computed tomography (micro-CT) data, which has also enabled tracking structural changes in response to externally applied loading in preclinical animal studies, contributing to a comprehensive description of both morphometric changes and mechanoregulation information of bone adaptation (Schulte et al. 2013, Birkhold et al. 2017, Albiol et al. 2020, San Cheong et al. 2020). Notably, with aging and in certain disease contexts, this remodeling process becomes unbalanced (Rubin et al. 1992, Bassey et al. 1998), often leading to further degenerative conditions such as osteoporosis, which precede an increased risk of fractures and culminate in considerable health and economic costs for society (Gabriel et al. 2002, Becker et al. 2010). An impaired bone mechanoregulation has been suggested as a possible cause of this problem. Therefore, advancing our ability to retrieve mechanoregulation information from time-lapsed *in vivo* micro-CT data can help better understand the underlying mechanisms and, with that, develop more effective treatments for these degenerative conditions.

In this regard, preclinical models, such as the mouse caudal vertebrae or tibia loading model, have been foundational to explore bone adaptation processes by enabling controllable experimental settings that can also mimic clinical pathological conditions (Rubin et al. 1994, Robling et al. 2002, Webster et al. 2008, Vandamme 2014, Razi et al. 2015, Roberts et al. 2019). As a result, existing methods to investigate mechanoregulation have successfully linked remodeling events with tissue strains obtained from micro-finite element (micro-FE) analysis, showing strong associations between formation/resorption and high/low tissue strains, respectively (Schulte et al. 2013, Razi et al. 2015, Scheuren et al. 2020), which were summarized in conditional probability curves defined over a continuous range of tissue strains. To this end, several mathematical quantities have been proposed to describe the local mechanical signal: strain energy density (SED), effective strain, and norm of the gradient of SED (∇SED). Deformation can be quantified using SED or effective strain (Pistoia et al. 2002), a derived quantity from SED that accounts for differences in tissue stiffness. Likewise, it is hypothesized that load-induced bone adaptation arises from mechanical deformation perceived by osteocytes, the mechanosensitive cells in bone (direct cell strain), and interstitial fluid flow (shear stress) in the lacunar-canalicular network (Klein-Nulend et al. 1995, Fritton et al. 2009, Weinbaum et al. 2011). Mathematically, ∇SED represents spatial differences in tissue deformation, which are believed to induce fluid flow (Huiskes 2000). From this perspective, it is unclear which mechanical signal shows the best association with bone remodeling events.

Furthermore, conditional probability-based approaches lack quantitative information describing the expected change in bone material for a given strain value. This dependency has been considered *in silico* (Levchuk et al. 2014, Goda et al. 2016, Louna et al. 2019) by defining the surface velocity in response to the perceived mechanical signals guiding remodeling events, analogous to the

mechanostat theory proposal. Besides, previous work has shown a dose-dependent effect of this mechanical stimulus (Mosley et al. 1998, Sugiyama et al. 2012, Scheuren et al. 2020, Walle et al. 2021), but an association of surface velocity with mechanical signal has not been investigated at the tissue level *in vivo*. On the one hand, it hinders more detailed comparisons of degenerative conditions that may conserve the mechanosensation ability of bone cells, associated with mechanical signal thresholds that regulate remodeling events, but influence the magnitude of the response to the mechanical stimuli and the overall bone turnover. On the other hand, from a computational modeling perspective, retrieving such information from *in vivo* data can provide valuable calibration data for the mechanoregulation mechanisms implemented in such models to achieve more realistic bone adaptation representations.

Therefore, the present study had two aims. First, we sought to identify which mechanical signal showed the best association with bone remodeling events using conditional probability curves and quantified with the correct classification rate (CCR) (Tourolle né Betts et al. 2020). Second, we aimed to propose a method to retrieve mechanoregulation information from time-lapsed *in vivo* micro-CT data that associates the surface remodeling velocity (RmV) with the local mechanical signal. We express this relationship in RmV curves from which several biologically meaningful parameters can be derived, such as formation/resorption thresholds and saturation levels. Notably, a consistent nomenclature of these parameters is proposed and formalized in alignment with the current understanding of the mechanostat theory. Furthermore, we applied our novel method to an *in vivo* mouse caudal vertebrae dataset (Scheuren et al. 2020) and quantified the local dynamic response of trabecular bone adaptation to static and cyclic loading of varying frequencies. We hypothesized that the effect of increased loading frequencies could be measured with our new analysis and compared through the parameters derived from these RmV curves. Finally, we investigated if there was a relationship between these parameters and loading frequency, analogous to the logarithmic relationship observed between loading frequency and net change in bone volume fraction over the 4-week observation period (Scheuren et al. 2020).

Materials and Methods

Time-lapsed *in vivo* micro-CT mouse caudal vertebrae dataset

The experimental data used for this study was collected in a previous longitudinal murine *in vivo* loading study (Scheuren et al. 2020), supporting 3R principles. Briefly, 11-week-old female C57BL/6J mice received surgery to allow mechanical loading of the sixth caudal vertebrae (CV6) via stainless steel pins (Fine Science Tools, Heidelberg, Germany) inserted into the fifth and seventh vertebrae following the protocol by Webster et al. (2008). After surgery and recovery, the 15-week-old mice were split into five groups: sham loading (0 N), 8 N static, or 8 N cyclic loading with the frequencies of 2 Hz, 5 Hz, or 10 Hz. The loading regime was performed for five minutes, three times per week, over four weeks, as previously described by Lambers et al. (2011). With the start of loading, the animals were scanned weekly using *in vivo* micro-CT (vivaCT 40, Scanco Medical AG, Switzerland), with an isotropic voxel size of 10.5 µm.

Automated compartmental analysis of the mouse caudal vertebrae

Consecutive time-points of the micro-CT scans were initially registered to each other using the Image Processing Language (IPL Version 5.04c; Scanco Medical AG, Switzerland). For the identification of the trabecular and cortical compartments in the structure, the images were filtered with a Gaussian filter (sigma: 1.2, truncate: 1) as implemented in (Virtanen et al. 2020), binarized with a threshold of 580 mgHA/cm^3 (Scheuren et al. 2020), followed by automatic identification of the relevant

compartments following the protocol proposed by Lambers et al. (2011). This approach was implemented in Python (version 3.9.9) and validated against the existing pipeline in IPL (Supplementary Material 1.1.1).

Micro-finite element analysis

Micro-CT images were analyzed with micro-finite element analysis (micro-FE) to estimate the local mechanical signal. The simulations computed strain energy density (SED, in MPa) in the vertebrae, from which all derived quantities were determined after rescaling to match the forces applied *in vivo*: 8 N for loaded groups and 4 N (physiological loading) for the sham-loaded group (0 N) (Christen et al. 2012). Two sets of simulations were performed for each sample: with homogeneous and heterogeneous material properties based on the binary and grayscale images of the samples. The former considered a Young's modulus value of 14.8 GPa for bone and a Poisson's ratio of 0.3 (Webster et al. 2008), whereas the latter applied the linear relationship between bone mineral density and Young's modulus in trabecular bone (Mulder et al. 2007), also using a Poisson's ratio of 0.3. Image voxels were converted to 8-node hexahedral elements, and bone was assumed to behave within the linear elastic regime. Two cylindrical discs were added at the proximal and distal ends of the vertebra model (Webster et al. 2008), mimicking the role of the intervertebral discs. Disc settings were calibrated for micro-FE with homogeneous and heterogeneous material properties (Supplementary Material 1.2). The nodes at the proximal end of the micro-FE mesh were constrained in all directions, while the nodes at the distal end were displaced by 1% of the length in the z-axis (longitudinal axis of the sample). The pipeline was also implemented in Python, and the simulations ran on the Euler cluster operated by Scientific IT Services at ETH Zurich, using the micro-FE solver ParOSol (Flaig et al. 2011) on Intel Xeon Gold 6150 processors (2.7-3.7 GHz).

Mechanoregulation analysis based on conditional probability curves

The mechanoregulation analysis performed in this study considered three mathematical quantities representing the local mechanical signal: strain energy density (SED), effective strain, and the norm of the gradient of SED (∇SED). In this context, the gradient was computed using the central difference scheme, and the norm was used as a proxy for the fluid flow in each voxel. For SED and effective strain, the values were collected on the voxels on the bone side of the surface interface between bone and marrow, while the values for ∇SED were collected on the marrow side.

The conditional probabilities of a remodeling event (formation, quiescence, resorption) to occur at each value of mechanical signal were calculated as described previously by Schulte et al. (2013), for weekly intervals and the 4-week observation period. The quantification of the amount of mechanoregulation information recovered in the analysis relied on the correct classification rate (CCR), using an implementation proposed by Tourolle né Betts et al. (2020), which summarizes in a single number the ability to accurately classify remodeling events within the range of observed local mechanical signal values.

Mechanostat remodeling velocity curve and parameter derivation

Here, we introduce a novel method to estimate sample-specific remodeling velocity curves and their corresponding mechanostat parameters based on time-lapsed micro-CT data. The proposed method considers the scans from two time-points: baseline and follow-up images. First, the follow-up image is registered to the baseline, revealing volumes of formed, quiescent, and resorbed clusters. Next, these clusters are used to classify surface voxels of the baseline image: formation surfaces consist of the overlap between dilated formed clusters and the baseline surface, resorption surfaces refer to the

overlap between resorbed clusters and the baseline surface, and quiescent surfaces contain the remaining surface voxels. A distance transform (DT) algorithm (taxicab metric) is applied to the follow-up image and the inverted follow-up image and masked with the formation and resorption surfaces identified before, yielding the distance of each surface voxel to the surface of the follow-up scan. It is assumed that the distance transform of the follow-up reveals the amount of formed bone, while the inverted follow-up identifies the depth of resorption per surface voxel. The values assigned to formation surfaces are obtained by gray-dilating the distance transform values of the formed clusters into the neighboring formation surface voxels identified. Further, these are linearly scaled in a cluster-specific fashion to match the volume of the corresponding cluster (Supplementary Figure 2). Next, the mechanical signal (ms) computed from the micro-FE analysis of the baseline image is collected using the same remodeling surface masks. Specifically, we selected effective strain in microstrain (με) as the mechanical signal descriptor.

Given that each surface voxel contains information on the amount of surface change and the estimated mechanical signal, a 2D histogram is computed, considering the mechanical signal on the horizontal axis and the estimated distance on the vertical axis. The mechanical signal is capped at the 99th percentile to eliminate very high (unphysiological) values, and the values are binned at 1% of this value. In the vertical axis, all values are considered and binned at 1% of the maximum value observed. A weighted average of the distance values is computed using the number of counts in the 2D histogram as weights, providing a value for each mechanical signal bin and considering a value of 0 for the quiescent surface voxels. The last step converts the estimated distance to a remodeling velocity magnitude by multiplying and dividing by the voxel size of the images and the interval between the time-points analyzed, respectively. For consistency with other dynamic morphometry quantities (such as mineral apposition and resorption rates), we chose to also express remodeling velocity in μm/day.

Finally, mathematical functions are fitted to the curves obtained, yielding their quantitative parametric description, namely: piecewise linear (Equation 1), as proposed in the original mechanostat theory, and a continuous hyperbola function (Equation 2), both illustrated in Figure 1, and which enable quantifying new remodeling parameters in vivo. The piecewise linear function is defined by formation and resorption saturation levels (FSL/RSL, μm/day) which determine the maximum and minimum remodeling velocities observed, formation and resorption thresholds (FT/RT, με) which determine the minimum/maximum mechanical signal value from which formation/resorption events are observed, and formation and resorption velocity modulus (FVM/RVM, μm/day / με) which determine the change in remodeling velocity resulting from a change in mechanical signal, defined between FSL/RSL and FT/RT, respectively. Specifically, we highlight the proposal to define FVM/RVM as a modulus, because the values are also proportional to mechanical strain. Comparably, the hyperbola function comprises similar FSL and RSL parameters, a remodeling threshold (RmT, μm/day) corresponding to the mechanical signal value at which the RmV curve is zero and a remodeling velocity modulus (RmVM, μm/day x με), which is defined as the scale factor determining the rate of change in remodeling velocity resulting from a change in mechanical signal.

Piecewise linear:

$$\text{RmV (ms)} = \begin{cases} \text{RSL, ms} < \text{RT} - \frac{\text{RSL}}{\text{RVM}} \\ -\text{RT} \times \text{RVM} + \text{RVM} \times \text{ms, RT} - \frac{\text{RSL}}{\text{RVM}} < \text{ms} < \text{RT} \\ 0, \text{RT} < \text{ms} < \text{FT} \\ -\text{FT} \times \text{FVM} + \text{FVM} \times \text{ms, FT} < \text{ms} < \text{FT} + \frac{\text{FSL}}{\text{FVM}} \\ \text{FSL, FT} + \frac{\text{FSL}}{\text{FVM}} < \text{ms} \end{cases} \quad \text{(Equation 1)}$$

Hyperbola function:

$$\text{RmV (ms)} = \text{FSL} - \frac{\text{RmVM}}{\text{RmT} + \text{ms}} \quad \text{(Equation 2)}$$

Note that for the hyperbola function, RSL is defined as the value of the RmV function at the minimum mechanical signal value observed.

The quality of the fits was assessed using the root mean squared error (RMSE) between the fitted curve and the corresponding velocity value at each mechanical signal value. The curve fitting was done with Scipy 1.7.3 (Virtanen et al. 2020) and Curve-fit annealing (Reinhardt 2019).

Frequency dependency of estimated mechanostat parameters

We implemented a balanced bootstrapping approach (Dvison et al. 1986) to characterize the distribution of the parameters estimated from the mathematical functions fitted to the remodeling velocity curves. Samples were randomly resampled 2500 times per group to generate a synthetic group of the same size, and the corresponding remodeling velocity curves were determined and fitted with the piecewise linear and hyperbola functions, yielding the estimations of the mechanostat parameters. We adopted the formula used previously (Scheuren et al. 2020) to evaluate the dependency of relevant parameters with cyclic loading frequency. Specifically, the median values of the distributions were plotted for each loading frequency and fitted with a logarithmic regression curve (Equation 3). The quality of the fit was assessed with the Pseudo-R^2 (Schabenberger et al. 2001) which allows comparing the quality of fitted relationships for parameters with different magnitudes.

$y = y_0 + \text{a} \times \ln(f)$, f represents the loading frequency (Equation 3).

Statistical analysis

Statistical analysis was performed with Python 3.10.5, using the packages SciPy 1.7.3 (Virtanen et al. 2020) and Scikit_posthocs 0.7.0 (Terpilowski 2019), and in R (R Core Team 2022). The analysis of longitudinal measurements of bone structural parameters was performed through repeated measurements ANOVA (Scheuren et al. 2020), implemented as a linear mixed model from the lmerTEST package (Kuznetsova et al. 2017), after inspection of linear regression diagnostics plots. All other parameters were first checked for normality, using the Shapiro-Wilk test. Non-normally distributed parameters were presented as median and inter-quartile range, while the remaining were presented as mean and standard deviation. Subsequently, parametric (one-way ANOVA followed by Tukey HSD) and non-parametric tests (Mann-Whitney U-test; Kruskal-Wallis followed by Conover-Iman test for multiple comparisons, corrected by Holm-Bonferroni method) were chosen based on the result of the normality test and indicated accordingly for each comparison. Mechanostat

parameter distributions generated by bootstrapping were compared using the Kolmogorov Smirnov test. Significance was set at $p < 0.05$ in all experiments, otherwise significance levels are reported.

Results

Performance comparison of mechanical signal descriptors for mechanoregulation analysis

First, we extended previous results (Scheuren et al. 2020) by comparing SED, effective strain and ∇SED and their ability to quantify mechanoregulation information from time-lapsed *in vivo* micro-CT data. Figure 2A illustrates the conditional probability curves for each combination of mechanical signal and group between weeks 0-4. This qualitative evaluation highlighted that, for all mechanical signal descriptors, resorption was tightly regulated within a small interval of low mechanical signal values (normalized mechanical signal < 10% for SED and ∇SED and normalized mechanical signal < 29% for effective strain), where it was associated with a higher conditional probability of occurrence. Furthermore, for higher magnitudes of the mechanical signal, the conditional probability curve displayed a more stochastic pattern oscillating around 0.33 for SED and ∇SED and stabilizing below this value for effective strain. ∇SED provided the best discriminative ability for formation and quiescence events for all groups, supported by statistically significant differences when comparing the difference between the conditional probability associated with formation and quiescence between the mechanical signal descriptors ($p<0.001$ for ∇SED-SED, ∇SED-effective strain and SED-effective strain). This was also substantiated by the increasing separation between both curves with an increase in mechanical signal magnitude (Figure 2A). The 10 Hz group achieved the widest difference between these events with 38% for ∇SED, in comparison to 33% for SED and 20% for effective strain, respectively, while the sham-loaded group showed a maximum difference of 33%, 24% and 12% for ∇SED, SED and effective strain, respectively. Conversely, effective strain was the best descriptor for resorption events based on the sharp increase in the conditional probability for this event within the interval of low mechanical signal values (normalized mechanical signal < 29%), reaching its maximum conditional probability value between 64% (2 Hz group) and 80% (static and 5 Hz groups), contrasting with values ranging between 47% (sham-loaded group) and 52% (5 Hz group) for ∇SED.

CCR was computed from the conditional probability curves, as a proxy of the amount of mechanoregulation information retrieved, quantifying the number of remodeling events which were correctly classified. Our analysis showed that ∇SED consistently achieved the best performance for the micro-FE analysis with homogeneous material properties, followed by effective strain and SED (Figure 2B). Across all groups and all timepoints, CCR values for ∇SED were significantly higher than those of SED (Figure 2B). A similar result was observed for ∇SED and effective strain, although no statistical differences were found for the loading frequencies groups of 5 Hz and 10 Hz after week 2 (Figure 2B). For the interval 0-4 weeks, CCR values for ∇SED were also significantly higher than those from SED ($p<0.001$) and effective strain ($p<0.05$) for all groups except for the 10 Hz group (Table 1). The effect of increasing loading frequencies was also noticeable in the corresponding increase in CCR values in the same period (Table 1). Conversely, for the micro-FE analysis with heterogeneous material properties, effective strain showed the best association with remodeling events, followed by SED and ∇SED, albeit the accuracy was lower than what was observed for micro-FE with homogeneous material properties, both in the weekly analysis (Figure 2B) and between 0-4 weeks (Table 1). Furthermore, there was a weaker increasing trend of CCR values with increasing loading frequencies (Table 1) in comparison to the micro-FE analysis with homogeneous material properties.

289 **Quantification of remodeling velocity curves and mechanostat parameters**

290 Next, we investigated bone mechanoregulation from time-lapsed *in vivo* micro-CT data by deriving
291 remodeling velocity curves and fitting piecewise linear and hyperbola functions to estimate the
292 corresponding mechanostat parameters, namely formation and resorption saturation levels
293 (FSL/RSL), velocity modulus (FVM/RVM) and thresholds (FT/RT) for the piecewise linear function
294 and FSL/RSL, remodeling velocity modulus (RmVM) and remodeling thresholds (RmT) for the
295 hyperbola function, respectively. We analyzed consecutive pairs of scans (Figure 3, Supplementary
296 Table 1), one week apart and summarized the group differences over the four-week period of the
297 study (Table 2).

298 The raw net response curves shown in Figure 3 resemble the shape of the mechanostat schematic
299 proposed by Frost (2000) within the adapted and mild overload windows, providing a qualitative
300 validation of the output which evaluated supraphysiological cyclic loads applied to the mouse
301 vertebrae.

302 Increasing loading frequency led to an increased number of formation events in comparison to
303 resorption for a given strain value, which is visible as a linear translation of the derived curves
304 towards higher RmV values, with formation events starting from lower mechanical signal threshold
305 values (Figure 3). Quantitatively, the parameters derived from the fitted curves showed an increase in
306 the FSL and decreased RT and RmT values with increasing loading frequency for both the weekly
307 and the 0-4 weeks analysis (Table 2, Supplementary Table 1). Furthermore, the RSL values
308 decreased for increasing loading frequencies (Supplementary Table 1), especially for weeks 3-4.

309 The RmV curves also allowed characterizing time-lapsed bone adaptation for each group, where the
310 range of RmV values decreased weekly (Figure 3) and converged towards comparable values
311 between groups. Overall, this result indicated that the magnitude of the mechanical signal in weeks 3
312 and 4 no longer induced the same strong remodeling responses observed in the first two weeks. FSL
313 values followed a similar pattern for each group over the four weeks (Supplementary Table 1). In the
314 first week, the remodeling velocity curves highlighted the acute response to supraphysiological
315 loading, since most loaded groups did not reach a plateau at their FSL value, which only occurred in
316 subsequent time-points. This progression was visible in the raw net response curves and in the fitted
317 mathematical functions (Figure 3). Concurrently, RVM and FVM values (Supplementary Table 1)
318 increased over time such that, at weeks 0-1, only regions of either high or low effective strain could
319 elicit the strongest response associated with the estimated formation and resorption saturation levels,
320 respectively. Over time, as the bone structure adapted to supraphysiological loading, the extent of
321 regions of either high or low effective strain decreased, also visible in the decrease in the range of
322 mechanical signal values (except for the sham-loaded group), and RSL and FSL were reached for
323 lower mechanical signal values (Figure 3, Supplementary Table 1). The remodeling velocity curves
324 showed that even highly loaded groups evolved from a state of predominant formation in the first two
325 weeks towards physiological remodeling conditions, where resorption is tightly regulated within an
326 interval of low mechanical signals and in agreement with the conditional probability curves shown
327 previously (Figure 2). These observations were also corroborated by an increase in Pearson
328 correlation coefficients between net remodeling curves of 5 Hz and 10 Hz loaded groups and the
329 sham-loaded group. Specifically, these increased from 0.828 and 0.822 ($p<0.0001$) for the weeks 0-1
330 to 0.908 and 0.883 ($p<0.0001$) between weeks 3-4, for the 5 Hz and 10 Hz groups, respectively,
331 supporting comparable bone remodeling responses between these groups except for their
332 mechanosensitivity, as seen in the differences between FT and RT values. A similar result was

observed for Pearson correlation coefficients between the 2 Hz and 10 Hz groups, and the 5 Hz and 10 Hz, increasing from 0.872 and 0.874 to 0.899 and 0.925, respectively.

Static loading still induced an anabolic response in the first week, characterized by a higher FSL in comparison to the sham-loaded group (Figure 3). However, in weeks 1-2 and 2-3, this group already matched the FSL values of the sham-loaded group suggesting a return to a physiological remodeling condition and eventually reached a lower FSL in week 3-4. RT and FT were visibly higher in the static group than in the sham-loaded group across all weeks, indicating that this loading condition still produced high strains in the structure.

Comparing the piecewise linear and hyperbola functions, the RMSE of the fitted curves indicated that these can be determined reliably and accurately, with an average RMSE of 0.357 and 0.314 µm/day for the former and latter, respectively, over the 4-week interval (Table 2) and yielding even lower RMSE values for the weekly analysis (Supplementary Table 1), partially given the lower magnitude of remodeling velocities observed. Additionally, lower RMSE values coupled with wider range of remodeling velocities obtained with the fitting of the hyperbola function suggested more accurate curve fits than with the piecewise linear function, which is especially crucial for the quantification of remodeling thresholds in the region where the remodeling velocity is zero (Figure 4A, Supplementary Table 1).

Finally, our analysis also investigated the trend followed by the mechanostat parameters derived from the fitted remodeling velocity curves with loading frequency. As shown in Figure 4B, a logarithmic function was suitable for several parameters estimated from the piecewise linear and hyperbolic fits (Figure 4B, Supplementary Table 2). For the piecewise linear function, FSL was accurately modeled by a logarithmic function across all time-points (Supplementary Table 2, Figure 4B for the interval 1-2), especially from the week 1 onwards and including between weeks 0-4. Additionally, FT values also followed the same trend for weeks 0-1 and 1-2, while RT showed the same behavior for all weekly time-points between week 1 and 4 (Supplementary Table 2). Similarly, for the hyperbola function, FSL was also accurately modeled by a logarithmic function across all time-points and weeks 0-4 (Supplementary Table 2, Figure 4B for the interval 1-2). RmT also followed a logarithmic relationship until week 2, analogous to the FT estimated with the piecewise linear function. Furthermore, all distributions generated for the fitted parameters were statistically significant from each other ($p<0.0001$, based on Kolmogorov-Smirnov test with Bonferroni correction for multiple comparisons), reinforcing the different responses to loading frequency.

Discussion

The present study aimed at evaluating mechanoregulation in trabecular bone adaptation and quantitatively characterizing the effects of loading frequencies on bone adaptation using a novel method to estimate remodeling velocity curves and their mechanostat parameters from time-lapsed *in vivo* mouse vertebra micro-CT data. Crucially, we showed that such RmV curves can be accurately determined and that several parameters obtained from them followed a logarithmic relationship with loading frequency, further supporting the trend observed previously for the change in bone volume fraction over the 4-week observation period (Scheuren et al. 2020).

First, we consolidated key factors that yield the best association between mechanical stimuli and local bone remodeling using existing methods for mechanoregulation analysis. Our results revealed that micro-FE analysis with homogeneous material properties achieved the best performance in recovering mechanoregulation information. Indeed, previous work on the murine tibia (Oliviero et al.

2021) has shown that micro-FE analysis with homogeneous material properties achieved the highest correlation between experimental and estimated material properties, while micro-FE with heterogeneous material properties of the lumbar vertebra L6 did not improve the prediction of failure force in comparison to homogeneous material properties (Harris et al. 2020). In any case, other applications where more significant changes in bone mineralization are expected, such as during fracture healing of cortical bone in the mouse femur (Tourolle né Betts et al. 2020), were more accurately modeled with heterogeneous material properties. Specifically, a "multi-density threshold approach" (Tourolle né Betts et al. 2020) implemented to assess bone mechanoregulation in fracture healing indicated that subsequent mechanoregulation analysis could leverage the heterogeneous properties assigned during the micro-FE to achieve a more detailed characterization of this mechanobiological process. Still, in the context of load-induced trabecular bone adaptation as explored in this work, the micro-CT images did not show large dynamic ranges in bone mineralization and changes in bone volume (Lambers et al. 2011, Oliviero et al. 2021), suggesting that the use of homogeneous material properties in micro-FE analysis is appropriate to model mechanically driven bone adaptation.

From a mathematical modeling perspective, the mechanostat theory (Frost 1987) is an established paradigm to describe bone adaptation in response to mechanical loading that has also been successfully applied in preclinical *in silico* models (Levchuk et al. 2014, Pereira et al. 2015, San Cheong et al. 2020, San Cheong et al. 2020). The analysis proposed in this work enables a direct estimation of such a relationship from time-lapsed *in vivo* micro-CT data and can be applied in a sample-specific or group-wise fashion and for an arbitrary time interval between the input images. We also proposed a nomenclature of mechanostat parameters, unifying the descriptions used in previous studies. For instance, the change in bone material in response to mechanical loading was originally named bone turnover and bone growth by Frost (1987), and later adapted to growth velocity using a detailed mathematical framework *in silico* (Levchuk et al. 2014, Goda et al. 2016, Louna et al. 2019). Here, we opted for remodeling velocity which fits the context of bone adaptation where there can be negative and positive growth, commonly termed remodeling (Hadjidakis et al. 2006). Conversely, formation/resorption thresholds and saturation levels were consistent with previous approaches (Levchuk et al. 2014, San Cheong et al. 2020). Regarding the change of RmV with mechanical signal, it was appropriate to align this term with the naming structure of the remaining parameters and provide an intuitive, succinct description integrating a modulus terminology: formation/resorption/remodeling velocity modulus. In this way, we aimed to strengthen the association of these terms with the mechanical signals, as modulus is inherently linked with other mechanical terms that relate a change in a quantity with a change in mechanical strain such as Young's modulus, describing the relationship between stress and strain for a given material.

Skerry (2006) stated that different loading conditions, such as those induced *in vivo* through varying loading frequencies, produce deviations to the habitual strain stimuli of the structure. Furthermore, he argued that different anatomical sites have specific "customary strain stimulus (CSS)" values to which the structure adapts. Our results align with these beliefs, where different loading frequencies produced significantly different responses (Scheuren et al. 2020), and the RmV curves evolved towards a state where remodeling thresholds were very close, suggesting a return to the habitual mechanostat rule and its local CSS value. For this reason, it is understandable that FT and RmT were no longer logarithmic dependent on loading frequency at week 4. Conversely, RT conserved a logarithmic trend with loading frequency for all weeks, which aligns with the tight regulation of resorption events observed in conditional probability and RmV curves. Crucially, an accurate derivation of the mechanostat curve required a calibration of the volume estimated for each remodeling cluster (Supplementary Figure 1A). For instance, smaller clusters with a high surface-to-

volume ratio were expectedly overestimated by the distance transform operation. This artifact is particularly noticeable for formation clusters where the identification of the neighboring surface from which they emerged requires a morphological dilation operation, leading to an increase in the number of surface voxels related to this event. While previous studies (Schulte et al. 2013, Razi et al. 2015, Scheuren et al. 2020) assessing bone mechanoregulation focused exclusively on conditional probabilities, which only consider the frequency of mechanical signal values per remodeling event, this volume correction becomes of significant importance in our proposed method, where a new axis focusing on the remodeling velocity at each voxel is considered and ultimately enabling the estimation of critical setpoints such as formation and resorption thresholds, where the RmV curve approaches zero. Importantly, the interval defined by these thresholds is typically described as a lazy zone, i.e., a range of strains where bone formation and resorption balance each other (Frost 1987).

In this regard, and in agreement with previous findings (Sugiyama et al. 2012, Schulte et al. 2013, Razi et al. 2015, San Cheong et al. 2020), our results provided no evidence of the existence of a lazy zone. This was further supported by the lower RMSE values associated with the fitted hyperbola mathematical functions which, by definition, cannot accommodate such an interval. Regardless, the estimated remodeling velocity curves agree with previous publications (Schulte et al. 2013, Razi et al. 2015), where resorption seems to be more tightly regulated than formation, based on the width of the interval of mechanical signal values allocated to each remodeling event, consistent for all groups and loading frequencies. Furthermore, the estimated remodeling rates, ranging between 0 and 3 µm/day, agree with the corresponding bone formation and resorption rates previously reported for this dataset (Scheuren et al. 2020) at around 2 µm/day, averaged across all remodeling clusters identified. Besides, the decreasing RSL values for increasing loading frequencies observed (Supplementary Table 1), especially for weeks 3-4, also align with previous work on the mouse tibia that showed an increase in the depth of resorption cavities with loading (Birkhold et al. 2017). Given the correction included in the curve estimation that ensures accurate volumes, established dynamic morphometry indices characterizing bone formation and resorption rates in a single value can now be expanded into a range of mechanical signals.

Nonetheless, there are some limitations to consider in this study. First, although the estimation of RmV curves can be determined in a sample-specific fashion, we observed that the analysis of group average curves was more reliable. These naturally contained more data points which were also filtered such that at least three samples were considered per mechanical signal value. Eventually, these factors were vital to produce relatively smooth RmV curves and enable consistent and plausible piecewise linear and hyperbola fits. In any case, as previous work has focused on group average results both *in vivo* (Schulte et al. 2013, Razi et al. 2015, San Cheong et al. 2020) and *in silico* (Levchuk et al. 2014, San Cheong et al. 2020, Boaretti et al. 2022), our analysis still aligns with such standard practices. Second, contrasting with conditional probability-based approaches, remodeling events are no longer characterized separately since our approach yields a single curve representing the average RmV for a given mechanical signal. Nonetheless, our goal was to derive a relationship in alignment with the mechanostat theory which, by definition, also does not describe remodeling events independently. Although conditional probability curves showed that these events can occur across the entire range of mechanical signals and highlight the interrelated effect of mechanical and biological cues governing targeted and non-targeted bone remodeling (Parfitt 2002, Schulte et al. 2013), we consider our approach complementary to this probability-based method. Furthermore, as different mechanical signal quantities performed differently for formation and resorption events, future approaches can attempt to combine both methods and derive separate RmV curves for formation and resorption using the mechanical signal that best associates with each event.

It should be noted that the current micro-CT image resolution challenges an accurate identification of sub-voxel phenomena. Indeed, such information would help to elucidate the assumption considered in our remodeling velocity estimation that the remodeling distance measured for each voxel surrounding a remodeling cluster can be linearly scaled to match the measured volume of the cluster. For the same reason, this factor also implies that the proposed method cannot recover single-cell behavior. Nonetheless, loading frequency was shown to be positively correlated with the number of osteocytes recruited in response to an increase in applied strain (Lewis et al. 2017), with a special focus on bone formation in a murine metatarsal model. Additionally, in a rat tibia model, increasing loading frequency was associated with a decrease in the estimated peak microstrain triggering periosteal bone formation and an increase in the rate of bone formation per microstrain (Hsieh et al. 2001). Combined, these results would emerge as an increase in FVM and a decrease in FT values with increasing frequency, which is indeed what our RmV curves show until week 3. Furthermore, the decreased anabolic response observed in the RmV curves for high strains may also be linked to a decrease in mechanosensitivity resulting from increased cell stiffness, as previously reported for such high strain values (Nawaz et al. 2012). Therefore, the trends estimated with the mechanostat remodeling velocity curves could be leveraged by *in silico* simulations that also rely on time-lapsed *in vivo* micro-CT data as input, such as novel agent-based models that simulate individual cell populations in 3D (Tourolle 2019, Boaretti et al. 2022) and with that, improve the accuracy of their predictions with respect to *in vivo* data. In this regard, our results demonstrating that several parameters estimated from the mechanostat also follow a logarithmic relationship with loading frequency can help to calibrate such models and investigate loading frequency-dependent responses *in silico*. With the advent of more powerful imaging methods, cell populations may soon be efficiently measured from *in vivo* samples and compared with the results of these *in silico* models. Additionally, our approach can support preclinical *in vivo* studies focusing on bone mechanoregulation. Previous work exploring the effects of aging and degenerative conditions described changes in conditional probabilities between young and aged groups (Razi et al. 2015), while studies focusing on pharmaceutical interventions characterized changes in global morphometry indices and micro-FE properties (Roberts et al. 2020). Therefore, investigating the effects of these conditions on remodeling thresholds (FT, RT, RmT) and remodeling modulus (FVM, RVM, RmVM) could help to identify effective mechanisms to counter degenerative conditions and maximize the potential of pharmaceutical interventions.

In conclusion, we have presented a novel method to estimate remodeling velocity curves and their parameters from time-lapsed *in vivo* micro-CT data. Furthermore, we applied this approach to evaluate the effects of different loading frequencies on the time-lapsed changes of bone microarchitecture by quantifying critical parameters describing bone mechanoregulation, such as formation saturation levels and remodeling thresholds. Crucially, we reinforced previous results that revealed a logarithmic relationship of bone volume change with loading frequency by showing that the mechanostat parameters estimated from RmV curves, such as remodeling thresholds and formation/resorption saturation levels, are also logarithmically dependent on loading frequency. Altogether, we expect these results to support future *in silico* and *in vivo* studies comparing the effects of mechanical loading and pharmaceutical treatment interventions on bone mechanoregulation and bone adaptation and, ultimately, identify more effective treatment plans that can be translated into clinical settings.

Conflict of Interest

The authors declare that the research was conducted in the absence of any commercial or financial relationships that could be construed as a potential conflict of interest.

Author Contributions

Study design: FM, AS, RM. **Study conduct**: FM, DB, MW. **Data collection**: FM. **Data analysis**: FM. **Data interpretation**: FM, DB, FS, RM. **Drafting manuscript**: FM. **Revising manuscript content**: FM, DB, MW, AS, FS, RM. **Approving final version of manuscript**: FM, DB, MW, AS, FS, RM. RM takes responsibility for the integrity of the data analysis.

Funding

This manuscript was based upon work supported by the European Research Council (ERC Advanced MechAGE ERC-2016-ADG-741883).

1 Data Availability Statement

Data and code will be made available upon reasonable request.

References

Albiol, L., A. Buttner, D. Pflanz, N. Mikolajewicz, A. I. Birkhold, I. Kramer, M. Kneissel, G. N. Duda, S. Checa and B. M. Willie (2020). "Effects of Long-Term Sclerostin Deficiency on Trabecular Bone Mass and Adaption to Limb Loading Differ in Male and Female Mice." Calcif Tissue Int 106(4): 415-430.

Bassey, E. J., M. C. Rothwell, J. J. Littlewood and D. W. Pye (1998). "Pre- and postmenopausal women have different bone mineral density responses to the same high-impact exercise." J Bone Miner Res 13(12): 1805-1813.

Becker, D. J., M. L. Kilgore and M. A. Morrisey (2010). "The societal burden of osteoporosis." Curr Rheumatol Rep 12(3): 186-191.

Birkhold, A. I., H. Razi, G. N. Duda, S. Checa and B. M. Willie (2017). "Tomography-Based Quantification of Regional Differences in Cortical Bone Surface Remodeling and Mechano-Response." Calcif Tissue Int 100(3): 255-270.

Boaretti, D., F. C. Marques, C. Ledoux, A. Singh, J. J. Kendall, E. Wehrle, G. A. Kuhn, Y. D. Bansod, F. A. Schulte and R. Müller (2022). "Trabecular bone remodeling in the ageing mouse: a micro-multiphysics agent-based *in silico* model using cell-type-specific mechanomic profiles." bioRxiv: 2022.2011.2016.516723.

Burr, D. B., A. G. Robling and C. H. Turner (2002). "Effects of biomechanical stress on bones in animals." Bone 30(5): 781-786.

Christen, P., B. van Rietbergen, F. M. Lambers, R. Muller and K. Ito (2012). "Bone morphology allows estimation of loading history in a murine model of bone adaptation." Biomech Model Mechanobiol 11(3-4): 483-492.

De Souza, R. L., M. Matsuura, F. Eckstein, S. C. Rawlinson, L. E. Lanyon and A. A. Pitsillides (2005). "Non-invasive axial loading of mouse tibiae increases cortical bone formation and modifies trabecular organization: a new model to study cortical and cancellous compartments in a single loaded element." Bone 37(6): 810-818.

Dvison, A. C., D. V. Hinkley and E. Schechtman (1986). "Efficient bootstrap simulation." Biometrika 73(3): 555-566.

Flaig, C. and P. Arbenz (2011). "A scalable memory efficient multigrid solver for micro-finite element analyses based on CT images." Parallel Computing 37(12): 846-854.

Fritton, S. P. and S. Weinbaum (2009). "Fluid and Solute Transport in Bone: Flow-Induced Mechanotransduction." Annu Rev Fluid Mech 41: 347-374.

Frost, H. M. (1987). "The mechanostat: a proposed pathogenic mechanism of osteoporoses and the bone mass effects of mechanical and nonmechanical agents." Bone and mineral 2(2): 73-85.

Frost, H. M. (2000). "The Utah paradigm of skeletal physiology: an overview of its insights for bone, cartilage and collagenous tissue organs." J Bone Miner Metab 18(6): 305-316.

Gabriel, S. E., A. N. Tosteson, C. L. Leibson, C. S. Crowson, G. R. Pond, C. S. Hammond and L. J. Melton, 3rd (2002). "Direct medical costs attributable to osteoporotic fractures." Osteoporos Int 13(4): 323-330.

Goda, I., J.-F. Ganghoffer and G. Maurice (2016). "Combined bone internal and external remodeling based on Eshelby stress." International Journal of Solids and Structures 94-95: 138-157.

Hadjidakis, D. J. and Androulakis, II (2006). "Bone remodeling." Ann N Y Acad Sci 1092: 385-396.

Harris, D., K. Garrett, S. Uppuganti, A. Creecy and J. S. Nyman (2020). "The BALB/c mouse as a preclinical model of the age-related deterioration in the lumbar vertebra." Bone 137.

Hsieh, Y. F. and C. H. Turner (2001). "Effects of loading frequency on mechanically induced bone formation." Journal of Bone and Mineral Research 16(5): 918-924.

Huiskes, R. (2000). "If bone is the answer, then what is the question?" Journal of Anatomy 197: 145-156.

Huiskes, R., R. Ruimerman, G. H. van Lenthe and J. D. Janssen (2000). "Effects of mechanical forces on maintenance and adaptation of form in trabecular bone." Nature 405(6787): 704-706.

Kameo, Y., T. Adachi and M. Hojo (2011). "Effects of loading frequency on the functional adaptation of trabeculae predicted by bone remodeling simulation." J Mech Behav Biomed Mater 4(6): 900-908.

Klein-Nulend, J., A. van der Plas, C. M. Semeins, N. E. Ajubi, J. A. Frangos, P. J. Nijweide and E. H. Burger (1995). "Sensitivity of osteocytes to biomechanical stress in vitro." FASEB J 9(5): 441-445.

Kuznetsova, A., P. B. Brockhoff and R. H. B. Christensen (2017). "lmerTest Package: Tests in Linear Mixed Effects Models." Journal of Statistical Software 82(13): 1-26.

Lambers, F. M., F. A. Schulte, G. Kuhn, D. J. Webster and R. Muller (2011). "Mouse tail vertebrae adapt to cyclic mechanical loading by increasing bone formation rate and decreasing bone resorption rate as shown by time-lapsed in vivo imaging of dynamic bone morphometry." Bone 49(6): 1340-1350.

Lanyon, L. E. (1992). "Control of bone architecture by functional load bearing." J Bone Miner Res 7 Suppl 2: S369-375.

Levchuk, A., A. Zwahlen, C. Weigt, F. M. Lambers, S. D. Badilatti, F. A. Schulte, G. Kuhn and R. Muller (2014). "The Clinical Biomechanics Award 2012 - presented by the European Society of

Biomechanics: large scale simulations of trabecular bone adaptation to loading and treatment." Clin Biomech (Bristol, Avon) 29(4): 355-362.

Lewis, K. J., D. Frikha-Benayed, J. Louie, S. Stephen, D. C. Spray, M. M. Thi, Z. Seref-Ferlengez, R. J. Majeska, S. Weinbaum and M. B. Schaffler (2017). "Osteocyte calcium signals encode strain magnitude and loading frequency in vivo." Proceedings of the National Academy of Sciences of the United States of America 114(44): 11775-11780.

Louna, Z., I. Goda and J.-F. Ganghoffer (2019). "Homogenized strain gradient remodeling model for trabecular bone microstructures." Continuum Mechanics and Thermodynamics 31(5): 1339-1367.

Mosley, J. R. and L. E. Lanyon (1998). "Strain rate as a controlling influence on adaptive modeling in response to dynamic loading of the ulna in growing male rats." Bone 23(4): 313-318.

Mulder, L., J. H. Koolstra, J. M. den Toonder and T. M. van Eijden (2007). "Intratrabecular distribution of tissue stiffness and mineralization in developing trabecular bone." Bone 41(2): 256-265.

Nawaz, S., P. Sanchez, K. Bodensiek, S. Li, M. Simons and I. A. T. Schaap (2012). "Cell Visco-Elasticity Measured with AFM and Optical Trapping at Sub-Micrometer Deformations." Plos One 7(9).

Oliviero, S., M. Roberts, R. Owen, G. C. Reilly, I. Bellantuono and E. Dall'Ara (2021). "Non-invasive prediction of the mouse tibia mechanical properties from microCT images: comparison between different finite element models." Biomech Model Mechanobiol 20(3): 941-955.

Parfitt, A. M. (2002). "Targeted and nontargeted bone remodeling: relationship to basic multicellular unit origination and progression." Bone 30(1): 5-7.

Pereira, A. F., B. Javaheri, A. A. Pitsillides and S. J. Shefelbine (2015). "Predicting cortical bone adaptation to axial loading in the mouse tibia." Journal of the Royal Society Interface 12(110).

Pistoia, W., B. van Rietbergen, E. M. Lochmuller, C. A. Lill, F. Eckstein and P. Ruegsegger (2002). "Estimation of distal radius failure load with micro-finite element analysis models based on three-dimensional peripheral quantitative computed tomography images." Bone 30(6): 842-848.

R Core Team (2022). R: A Language and Environment for Statistical Computing, R Foundation for Statistical Computing.

Razi, H., A. I. Birkhold, R. Weinkamer, G. N. Duda, B. M. Willie and S. Checa (2015). "Aging Leads to a Dysregulation in Mechanically Driven Bone Formation and Resorption." J Bone Miner Res 30(10): 1864-1873.

Reinhardt, S. (2019). "Curve fit annealing." Retrieved 11/08/2022, from https://github.com/amba/curve_fit.annealing.

Roberts, B. C., H. M. A. Carrera, S. Zanjani-pour, M. Boudiffa, N. Wang, A. Gartland and E. Dall'Ara (2020). "PTH(1-34) treatment and/or mechanical loading have different osteogenic effects on the trabecular and cortical bone in the ovariectomized C57BL/6 mouse." Scientific Reports 10(1).

Roberts, B. C., M. Giorgi, S. Oliviero, N. Wang, M. Boudiffa and E. Dall'Ara (2019). "The longitudinal effects of ovariectomy on the morphometric, densitometric and mechanical properties in the murine tibia: A comparison between two mouse strains." Bone 127: 260-270.

Robling, A. G. and C. H. Turner (2002). "Mechanotransduction in bone: genetic effects on mechanosensitivity in mice." Bone 31(5): 562-569.

Rubin, C. T., S. D. Bain and K. J. McLeod (1992). "Suppression of the osteogenic response in the aging skeleton." Calcif Tissue Int 50(4): 306-313.

Rubin, C. T. and K. J. McLeod (1994). "Promotion of bony ingrowth by frequency-specific, low-amplitude mechanical strain." Clin Orthop Relat Res(298): 165-174.

San Cheong, V., A. C. Marin, D. Lacroix and E. Dall'Ara (2020). "A novel algorithm to predict bone changes in the mouse tibia properties under physiological conditions." Biomechanics and Modeling in Mechanobiology 19(3): 985-1001.

San Cheong, V., B. C. Roberts, V. Kadirkamanathan and E. Dall'Ara (2020). "Bone remodelling in the mouse tibia is spatio-temporally modulated by oestrogen deficiency and external mechanical loading: A combined in vivo/in silico study." Acta Biomaterialia 116: 302-317.

Schabenberger, O. and F. J. Pierce (2001). Contemporary Statistical Models for the Plant and Soil Sciences. Boca Raton, CRC Press.

Scheuren, A. C., P. Vallaster, G. A. Kuhn, G. R. Paul, A. Malhotra, Y. Kameo and R. Muller (2020). "Mechano-Regulation of Trabecular Bone Adaptation Is Controlled by the Local in vivo Environment and Logarithmically Dependent on Loading Frequency." Frontiers in Bioengineering and Biotechnology 8.

Schulte, F. A., D. Ruffoni, F. M. Lambers, D. Christen, D. J. Webster, G. Kuhn and R. Muller (2013). "Local Mechanical Stimuli Regulate Bone Formation and Resorption in Mice at the Tissue Level." Plos One 8(4).

Skerry, T. M. (2006). "One mechanostat or many? Modifications of the site-specific response of bone to mechanical loading by nature and nurture." J Musculoskelet Neuronal Interact 6(2): 122-127.

Sugiyama, T., L. B. Meakin, W. J. Browne, G. L. Galea, J. S. Price and L. E. Lanyon (2012). "Bones' adaptive response to mechanical loading is essentially linear between the low strains associated with disuse and the high strains associated with the lamellar/woven bone transition." Journal of Bone and Mineral Research 27(8): 1784-1793.

Terpilowski, M. (2019). "scikit-posthocs: Pairwise multiple comparison tests in Python." Journal of Open Source Software 4(36).

Tourolle, D. (2019). A micro-scale multiphysics framework for fracture healing and bone remodelling. D-HEST, ETH Zurich. Doctoral Degree.

Tourolle né Betts, D. C., E. Wehrle, G. R. Paul, G. A. Kuhn, P. Christen, S. Hofmann and R. Müller (2020). "The association between mineralised tissue formation and the mechanical local in vivo environment: Time-lapsed quantification of a mouse defect healing model." Sci Rep 10(1100).

Turner, C. H. (1998). "Three rules for bone adaptation to mechanical stimuli." Bone 23(5): 399-407.

Vandamme, T. (2014). "Use of rodents as models of human diseases." Journal of Pharmacy And Bioallied Sciences 6(1): 2-9.

Virtanen, P., R. Gommers, T. E. Oliphant, M. Haberland, T. Reddy, D. Cournapeau, E. Burovski, P. Peterson, W. Weckesser, J. Bright, S. J. van der Walt, M. Brett, J. Wilson, K. J. Millman, N. Mayorov, A. R. J. Nelson, E. Jones, R. Kern, E. Larson, C. J. Carey, I. Polat, Y. Feng, E. W. Moore, J. VanderPlas, D. Laxalde, J. Perktold, R. Cimrman, I. Henriksen, E. A. Quintero, C. R. Harris, A. M. Archibald, A. H. Ribeiro, F. Pedregosa, P. van Mulbregt and C. SciPy (2020). "SciPy 1.0: fundamental algorithms for scientific computing in Python." Nat Methods 17(3): 261-272.

Walle, M., F. C. Marques, N. Ohs, M. Blauth, R. Muller and C. J. Collins (2021). "Bone Mechanoregulation Allows Subject-Specific Load Estimation Based on Time-Lapsed Micro-CT and HR-pQCT in Vivo." Frontiers in Bioengineering and Biotechnology 9.

Webster, D. J., P. L. Morley, G. H. van Lenthe and R. Muller (2008). "A novel in vivo mouse model for mechanically stimulated bone adaptation--a combined experimental and computational validation study." Comput Methods Biomech Biomed Engin 11(5): 435-441.

Weinbaum, S., Y. Duan, M. M. Thi and L. You (2011). "An Integrative Review of Mechanotransduction in Endothelial, Epithelial (Renal) and Dendritic Cells (Osteocytes)." Cell Mol Bioeng 4(4): 510-537.

Wolff, J. (1986). The law of bone remodeling. Maqet P., Furlong R., (Translation), Berlin, Germany: Springer Verlag.

Figure captions

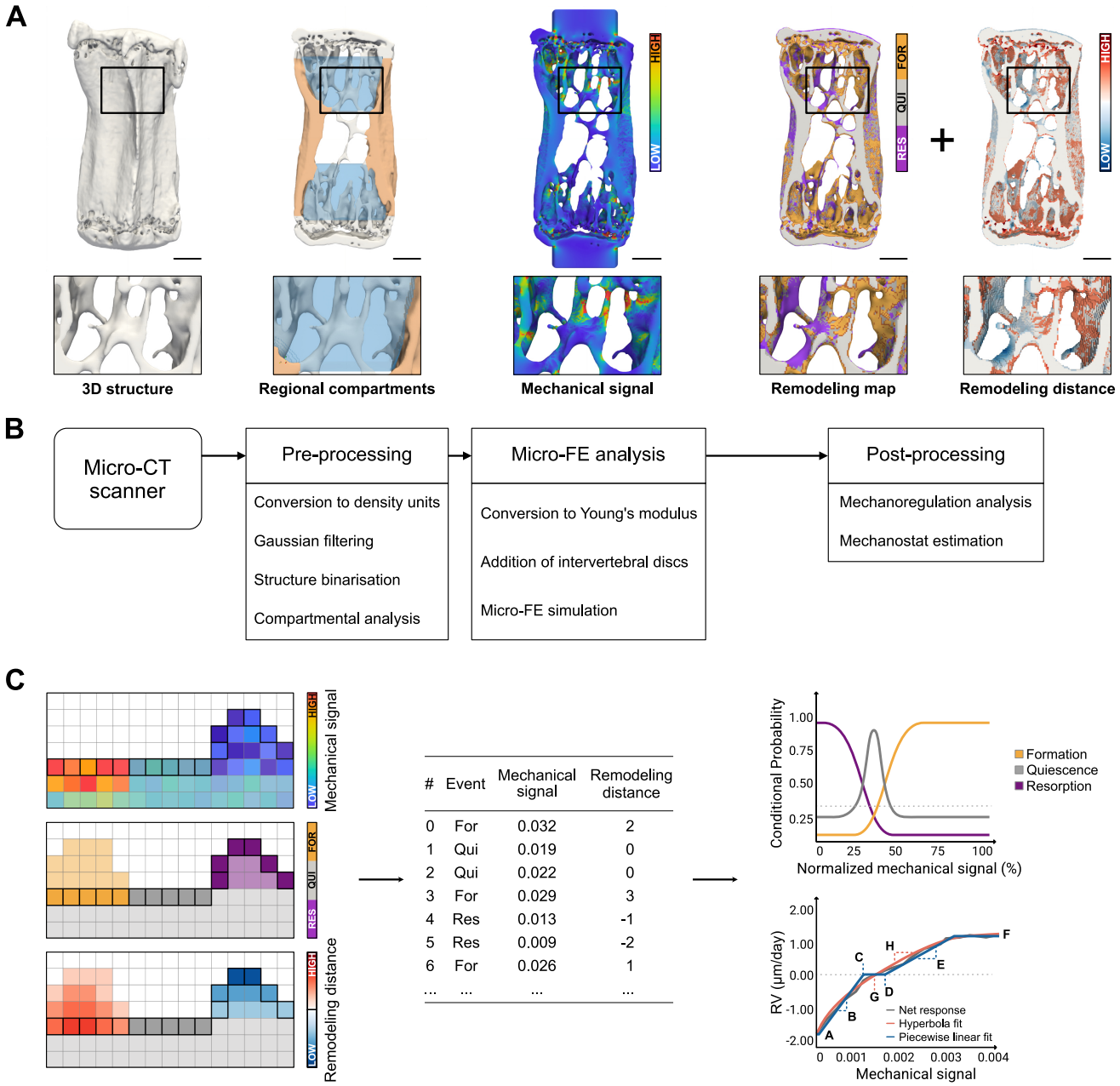

Figure 1

Overview of the computational pipeline for high-throughput analysis of time-lapsed *in vivo* micro-CT mouse caudal vertebra samples. A) Qualitative visualization of representative samples highlighting the original bone structure, the identification of regional compartments (trabecular compartment in blue and cortical compartment in orange), the local mechanical signal computed as strain energy density (SED) from micro-FE analysis, the remodeling map obtained from time-lapsed micro-CT images and the remodeling distance associated with surface voxels (Scale bar: 500 µm). B) Diagram of the workflow included in the computational pipeline, starting from pre-processing of micro-CT images to post-processing steps, featuring mechanoregulation analysis. C) Illustration of the workflow for mechanoregulation analysis and estimation of mechanostat parameters: for each surface voxel, remodeling events are identified by overlapping consecutive time-points, the mechanical signal in the structure is computed with micro-FE and the remodeling distance is determined with a

distance transform operation (see Materials and Methods). The data is used to compute conditional probability curves for each remodeling event (dashed line represents a random probability of occurrence) and a remodeling velocity curve (dashed line represents zero remodeling velocity), which can be fitted with a piecewise linear function or a continuous hyperbola function to retrieve biologically meaningful parameters. Parameter legend (see Materials and Methods for an extended description): A- Resorption saturation level (RSL), B- Resorption velocity modulus (RVM), C- Resorption threshold (RT), D- Formation threshold (FT), E- Formation velocity modulus (FVM), F- Formation saturation level (FSL), G- Remodeling threshold (RmT), H- Remodeling velocity modulus (RmVM).

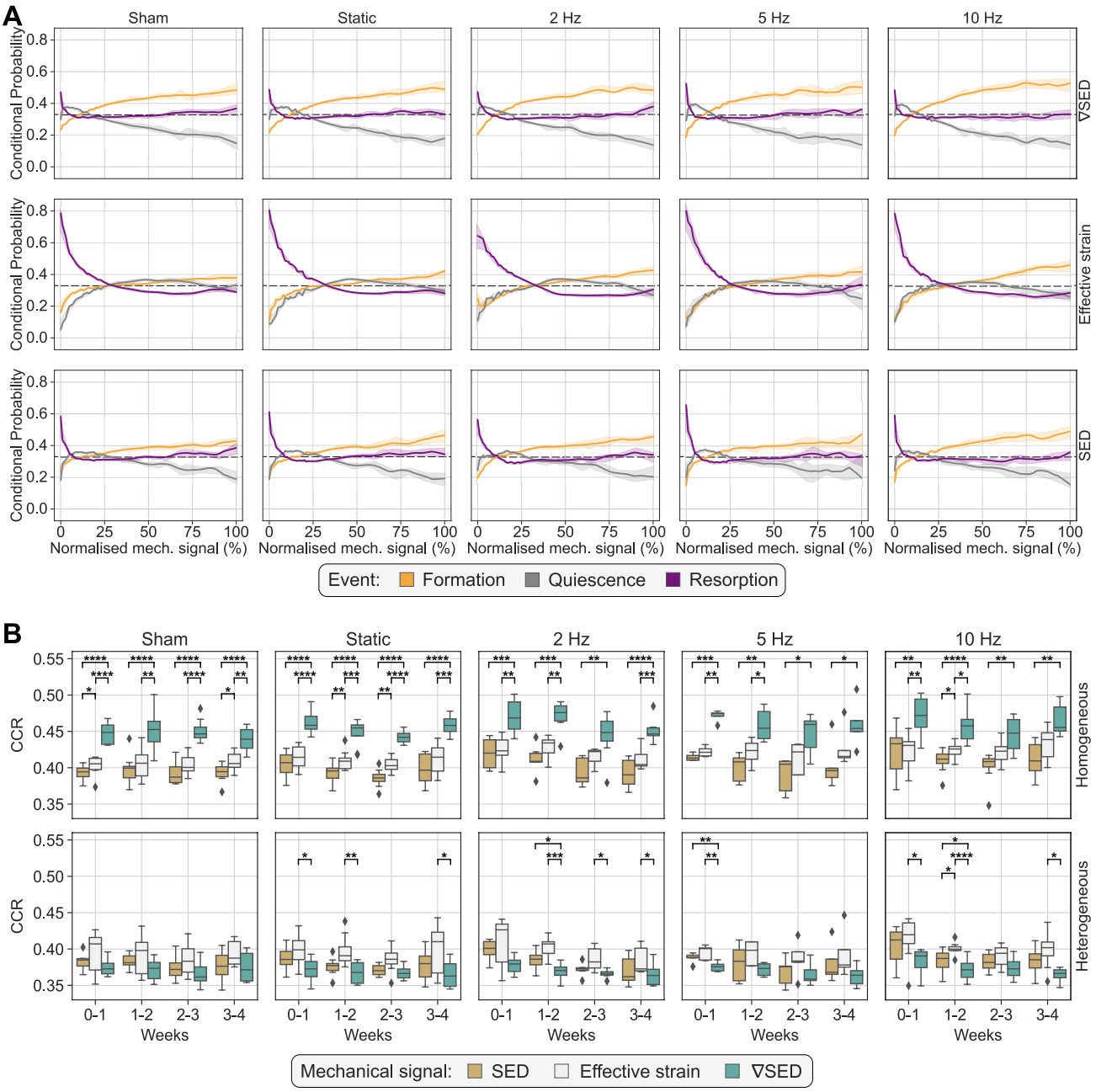

Figure 2

712 Quantification of mechanoregulation information from time-lapsed *in vivo* micro-CT image data. A)
713 Conditional probability curves connecting the mechanical environment with remodeling events,
714 computed for all groups and mechanical signal descriptors considered (SED, effective strain and
715 ∇SED). The plots show the mean probability line per group after applying a LOWESS operation for
716 the interval 0-4 weeks and its corresponding 95% confidence interval. Dashed line at 0.33 identifies
717 the probability of a random event for a ternary classification case. B) Comparison of correct
718 classification rate (CCR) values obtained by SED, effective strain and ∇SED as local mechanical
719 signal descriptors, computed from micro-FE with homogeneous or heterogeneous material properties.
720 Higher CCR values indicate higher sensitivity to retrieve mechanoregulation information. Statistical
721 significance determined by Conover-Iman test, corrected for multiple comparisons by Holm-
722 Bonferroni method. Statistical significance legend: *p < 0.05, **p < 0.01, ***p < 0.001, ****p <
723 0.0001.

724

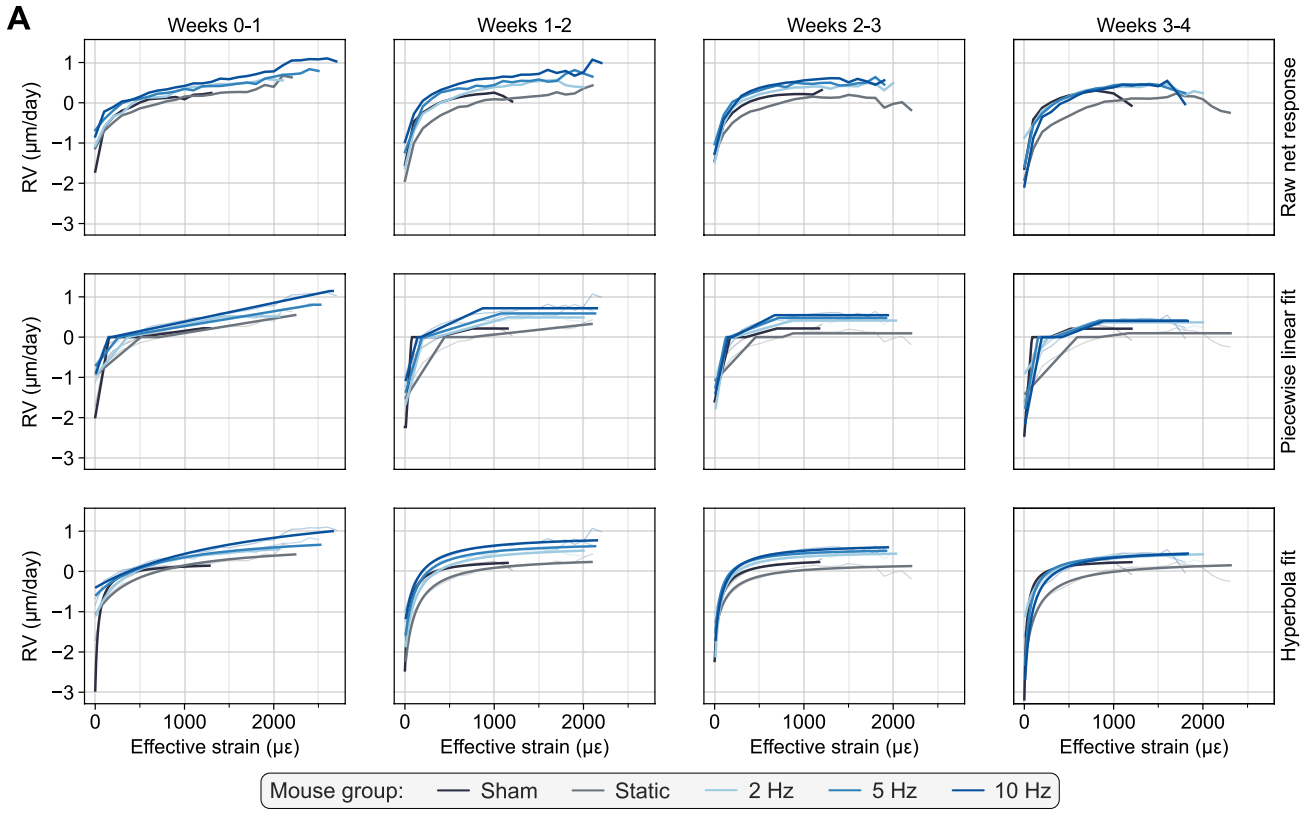

725

726 **Figure 3**

727 Estimation of the mechanostat remodeling velocity (RmV) curve from time-lapsed *in vivo* micro-CT
728 imaging data, illustrated with the average raw net response (top row) per group, the fitted piecewise
729 linear functions (middle row), as described in the mechanostat theory and continuous hyperbola
730 functions (bottom row) for the weeks 1-2. Data points are filtered such that at least three mice are
731 averaged for each mechanical signal value.

732

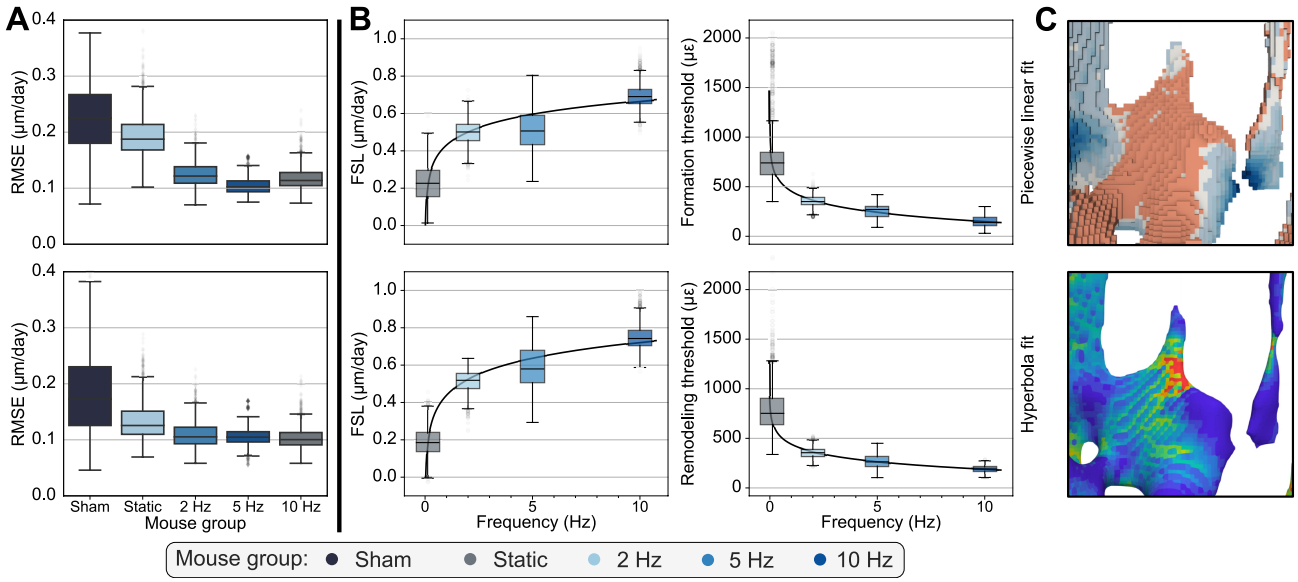

Figure 4

A) Root mean squared errors (RMSE) associated with the piecewise linear (top row) and hyperbola (bottom row) fitted functions are shown, highlighting that the hyperbola function consistently achieved lower errors than the piecewise linear function. B) Logarithmic relationships fitted to the bootstrapped distributions of mechanostat parameters estimated from the piecewise linear (top row) and hyperbola (bottom row) functions fitted to the remodeling velocity curves for the weeks 1-2. Formation saturation levels (FSL), formation and remodeling thresholds (FT and RmT) were among the parameters that follow a logarithmic trend throughout the 4 weeks of the study. C) Qualitative visualization linking remodeling distance measurements with the mechanical environments *in vivo* as effective strain.

Tables

Table 1

Correct classification rate (CCR) for all groups, mechanical signal descriptors and material properties analyzed, for the weeks 0-4. Data presented as "median (IQR)". Statistical significance legend: a – "SED – Effective strain", b – "Effective strain – ∇SED", c – "SED – ∇SED"; *p < 0.05, **p < 0.01, ***p < 0.001, ****p < 0.0001. Statistical significance determined with Conover's test corrected for multiple comparisons with step-down method using Bonferroni-Holm adjustments.

Material properties	Group	Mechanical signal			p-value
		SED	Effective strain	∇SED	
Homogeneous	Sham	0.378 (0.374 - 0.391)	0.400 (0.392 - 0.404)	0.421 (0.413 - 0.440)	*a, **b, ****c
	Static	0.389 (0.375 - 0.395)	0.405 (0.403 - 0.410)	0.434 (0.427 - 0.448)	*b, ***c

	02Hz	0.402 (0.387 - 0.404)	0.411 (0.407 - 0.417)	0.450 (0.430 - 0.451)	*b, ***c
	05Hz	0.396 (0.387 - 0.397)	0.404 (0.399 - 0.422)	0.446 (0.439 - 0.454)	*a, *b, ***c
	10Hz	0.417 (0.382 - 0.443)	0.418 (0.395 - 0.428)	0.461 (0.431 - 0.489)	ns
Heterogeneous	Sham	0.381 (0.373 - 0.387)	0.423 (0.410 - 0.432)	0.371 (0.366 - 0.374)	*b, **c
	Static	0.386 (0.379 - 0.392)	0.423 (0.416 - 0.434)	0.377 (0.364 - 0.381)	*b, **c
	02Hz	0.387 (0.387 - 0.397)	0.430 (0.399 - 0.434)	0.382 (0.375 - 0.391)	*b, **c
	05Hz	0.394 (0.387 - 0.398)	0.420 (0.412 - 0.431)	0.380 (0.372 - 0.391)	ns
	10Hz	0.397 (0.387 - 0.435)	0.427 (0.414 - 0.447)	0.395 (0.365 - 0.408)	ns

Table 2

Parameters of the mathematical functions fitted to the estimated mechanostat group average remodeling velocity curves for the interval weeks 0-4. Root mean squared error (RMSE) was used to characterize the quality of the fit. See Materials and Methods for an extended description of the parameters. The row "Effective strain range" indicates the range of mechanical signal values from which the fit of the mathematical functions was derived.

Function	Parameter	Unit	Group				
			Sham	Static	2Hz	5Hz	10Hz
Piecewise linear	RSL	μm/day	-4.305	-3.062	-1.729	-2.570	-4.112
	RVM ($x10^3$)	(μm/day) / με	29.748	5.737	8.802	16.245	45.003
	RT	με	145	544	246	187	101
	FT	με	440	1511	270	190	110
	FVM ($x10^3$)	(μm/day) / με	1.676	1.919	2.435	2.330	2.481
	FSL	μm/day	0.180	0.891	1.274	1.640	1.954
	RMSE	μm/day	0.381	0.382	0.227	0.407	0.388

Hyperbola	RSL	μm/day	-5.776	-4.115	-2.390	-3.208	-4.180
	RmVM ($x10^{-3}$)	(μm/day) x με	-0.236	-1.037	-0.843	-0.769	-0.507
	RmT	με	482	899	268	228	158
	FSL	μm/day	0.038	0.522	1.468	1.836	2.051
	RMSE	μm/day	0.274	0.347	0.226	0.372	0.350
Effective strain range		με	10–1280	10–2240	10–2060	10–2520	10–2650

759